Stem Cell Reports
Article

ISSCR

OPEN ACCESS

FOXO4-SP6 axis controls surface epithelium commitment by mediating epigenomic remodeling

Jiafeng Liu,[1,4] Huaxing Huang,[1,4] Fengjiao An,[1,4] Siqi Wu,[1] Huizhen Guo,[1] Bofeng Wang,[1] Zhuo Han,[1] Jieying Tan,[1] Zesong Lin,[1] Yihang Fang,[1] Jinpeng Liu,[1] Hanning Ye,[3] Yuru Du,[3] Kunlun Mo,[1] Ying Huang,[1] Mingsen Li,[1] Li Wang,[1] Zhen Mao,[1] and Hong Ouyang[1,2,5,*]

[1]State Key Laboratory of Ophthalmology, Zhongshan Ophthalmic Center, Sun Yat-sen University, Guangdong Provincial Key Laboratory of Ophthalmology and Visual Science, Guangzhou 510060, China
[2]Center for Stem Cell Biology and Tissue Engineering, Key Laboratory for Stem Cells and Tissue Engineering, Ministry of Education, Zhongshan School of Medicine, Sun Yat-Sen University, Guangzhou 510060, China
[3]Zhongshan School of Medicine, Sun Yat-Sen University, Guangzhou 510060, China
[4]These authors contributed equally
[5]Lead contact
*Correspondence: Ouyhong3@mail.sysu.edu.cn
https://doi.org/10.1016/j.stemcr.2025.102445

SUMMARY

Proper development of surface epithelium (SE) is a requisite for the normal development and function of ectodermal appendages; however, the molecular mechanisms underlying SE commitment remain largely unexplored. Here, we developed a KRT8 reporter system and utilized it to identify FOXO4 and SP6 as novel, essential regulators governing SE commitment. We found that the FOXO4-SP6 axis governs SE fate and its abrogation markedly impedes SE fate determination. Mechanistically, FOXO4 regulates SE initiation by shaping the SE chromatin accessibility landscape and regulating the deposition of H3K4me3. SP6, as a novel effector of FOXO4, activates SE-specific genes through modulating the H3K27ac deposition across their super-enhancers. Our work highlights the regulatory function of the FOXO4-SP6 axis in SE development, contributing to an improved understanding of SE fate decisions and providing a research foundation for the therapeutic application of ectodermal dysplasia.

INTRODUCTION

The development of the surface epithelium (SE) is a critical process in vertebrate embryogenesis, giving rise to essential structures such as epidermis, corneal and oral epithelium, as well as hair follicles and mammary glands (Biggs and Mikkola, 2014; Collomb et al., 2013; Di Girolamo and Park, 2023; Jones and Klein, 2013; Lwigale, 2015). Abnormalities in SE development can result in ectodermal dysplasia that impact the formation of complete structure and function of ectodermal appendages. For example, aberrations in the ectodysplasin pathway, a key signal for SE development, can lead to the dysplasia of skin, hair, teeth, and sweat glands (Itin, 2014; Kowalczyk-Quintas and Schneider, 2014; Yu et al., 2023). Defects in the WNT pathway during SE development result in the failure of ocular morphogenesis (Carpenter et al., 2015). Understanding the regulatory mechanisms governing this process is fundamental to developmental biology and has significant implications for regenerative medicine and congenital disorder research.

The cell fate decision is largely regulated by its surrounding microenvironmental cues, including the extracellular morphogens, cell-matrix interaction, and the dynamic of cell density (Kicheva and Briscoe, 2023; LeBlanc et al., 2022; Rauner and Kuperwasser, 2021). Numerous established human pluripotent stem cell (hPSCs) differentiation systems rely on precise modulation of these factors to achieve the induction of diverse lineages. The combined induction of retinoic acid (RA) and bone morphogenetic protein 4 (BMP4) efficiently induces the generation of SE cells (Li et al., 2019). Through the combined treatment of small molecules Activin A, BMP4, CHIR99021, and PD0325901 under conditions of high-density culture, hPSCs tend to adopt the SE fate rather than differentiate into the amniotic ectoderm (Nakanoh et al., 2024).

Super-enhancers are a large cluster of transcriptionally active enhancers bound by a high density of transcriptional and chromatin-modifying factors to drive the expression of key cell-type-specific genes and control cell identity (Adam et al., 2015; Hnisz et al., 2013; Whyte et al., 2013). Core transcription factors (TFs) control the chromatin reorganization, lineage-specific super-enhancer orchestration, and lineage-specific gene activation during lineage commitment (Shukla et al., 2022; Spitz and Furlong, 2012; Whyte et al., 2013; Zaret, 2020). Several transcriptional regulators have been reported to control SE development. Notably, mutation in GRHL2 is a common cause of autosomal-recessive ectodermal dysplasia syndrome (Petrof et al., 2014), while the absence of TFAP2A perturbs the ectodermal development and results in craniofacial malformation in mice (Van Otterloo et al., 2022). TFAP2C is indispensable for establishing interconnecting TF networks during SE commitment

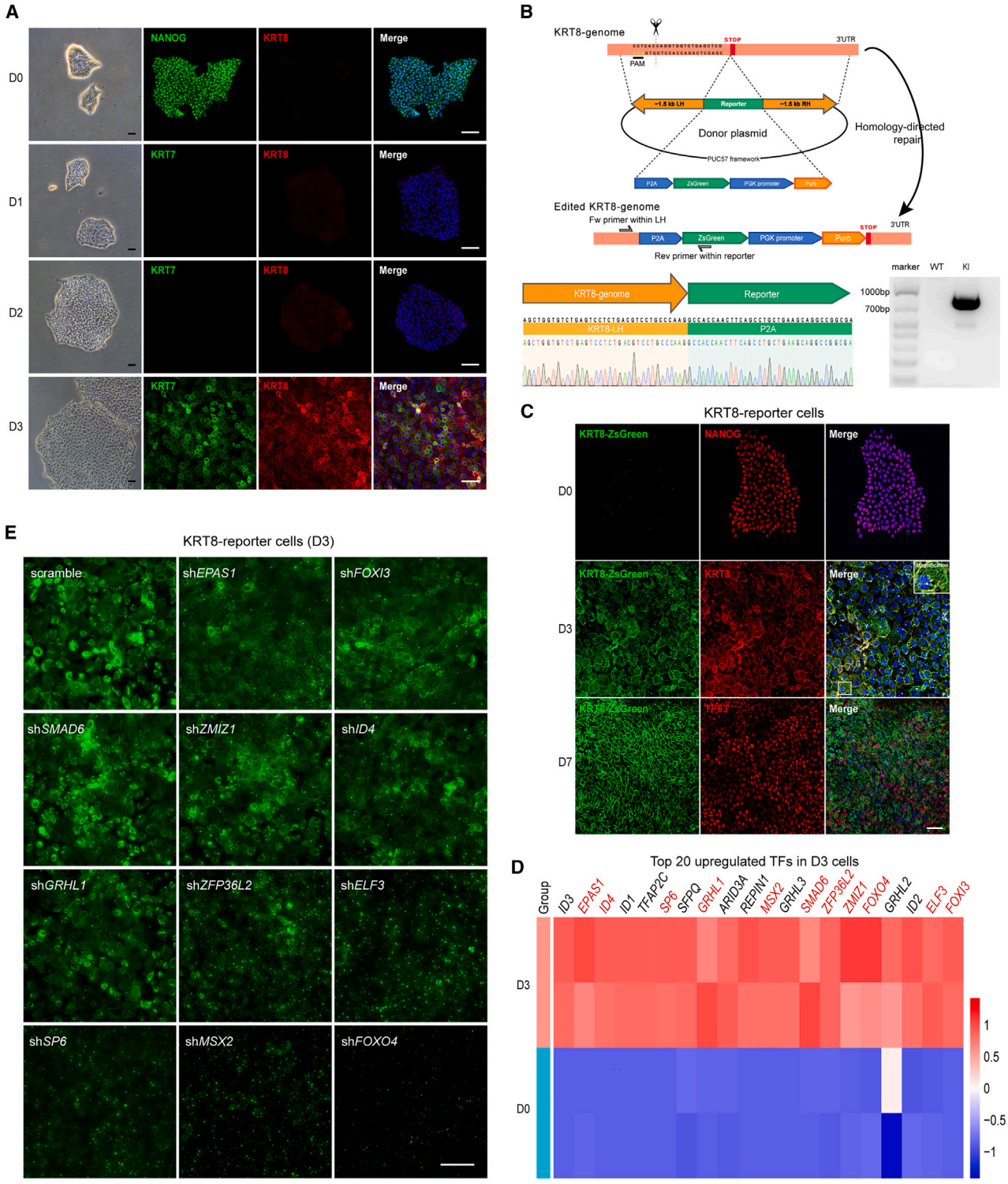

Figure 1. Generation of a KRT8 reporter hESC cell line and identification of candidate TFs

(A) Images of phase contrast and immunostaining for NANOG, KRT7, and KRT8 in the differentiated cells on D0, D1, D2, and D3. Scale bar, 100 μm.

(B) Top: schematic diagram of reporter cassette knockin into the KRT8 locus by CRISPR-Cas9-mediated genome editing. LH, left homologous arm; RH, right homologous arm. Bottom: Sanger sequencing of the edited KRT8 locus to confirm the precise insertion of the

(legend continued on next page)

(Li et al., 2019); GRHL3 acts as an initiation factor that primes the SE chromatin accessibility landscape and activates SE-specific genes (Huang et al., 2022). However, to date, the composition of SE lineage super-enhancers and the mechanism by which core TFs mediate the establishment of SE lineage super-enhancers remain unclear.

FOXO4, a member of the forkhead TF family, plays a crucial role in neural fate determination and T helper 1 cell differentiation (Chen et al., 2022; Vilchez et al., 2013). SP6, a member of the Sp family of TFs, exhibits indispensable functions in tooth morphogenesis and the generation of cytotrophoblasts (Chen et al., 2024; Rhodes et al., 2021; Ruspita et al., 2020). In this study, taking advantage of the KRT8 reporter system, we investigated a set of highly expressed TFs and identify that FOXO4 and SP6 coordinately regulate SE commitment. Depletion of the FOXO4-SP6 axis markedly blocked SE fate determination. FOXO4 mediates SE differentiation through modulating H3K4me3 deposition and establishing SE chromatin accessibility landscape. SP6, as a downstream effector of FOXO4, drives transcription of SE-specific genes via orchestrating the H3K27ac deposition across their super-enhancers. Our work elucidates the regulatory function of the FOXO4-SP6 axis in driving SE commitment, providing novel insights into the molecular mechanism underlying SE development and highlighting potential targets for therapeutic intervention in disorders related to ectodermal dysplasia.

RESULTS

Identify pivotal SE regulators using a KRT8 reporter system

To better decipher the underlying molecular mechanism involved in SE commitment, we have previously developed a robust model of directed differentiation of human embryonic stem cells (hESCs) into SE (Huang et al., 2024). The precise temporal framework during SE differentiation progression was defined by monitoring the dynamic changes in cell morphology, along with the expression of SE markers KRT7 and KRT8, and the epidermal master regulator TP63, which serves as a hallmark of matured SE (Figures 1A and S1A). We observed that during the progression of SE differentiation, the cells lost hESC morphology, transitioned to an epithelial-like morphology, and exhibited abundant expression of KRT7 and KRT8 on the third day of differentiation (D3) (Figure 1A). This observation led us to identify D3 as a critical transition stage marking the initiation of SE differentiation. As differentiation further progressed, the cells maintained their epithelial-like morphology and vigorously expressed TP63 on D7, demonstrating that the period from D4 to D7 represented the SE maturation phase (Figure S1A). We then sequentially induced the SE cells to differentiate into epidermal progenitors ($KRT5^+$, $KRT14^+$, and $TP63^+$) and terminally differentiated keratinocytes ($KRT1^+$ and $KRT10^+$) (Koster and Roop, 2007; Liu et al., 2013), and the epidermal progenitors formed stratified epidermal layers in an air-lifting culture system (Figures S1B and S1C), validating that the SE cells possess the developmental potential to differentiate into functional epidermal progenitors.

To dynamically monitor the progression of SE differentiation, and to uncover the critical TFs that are indispensable for the SE cell fate determination, we devised a reporter hESC cell line by CRISPR-based genome editing, which carries a ZsGreen fluorescent protein, strategically positioned under the regulatory control of KRT8, which serves as hallmark indicative of the successful transition to the SE lineage (Figure 1B). We confirmed the precise insertion of the reporter cassette through sequencing and PCR analysis (Figure 1B). Knockin of ZsGreen did not compromise the pluripotency maintenance or lead to cellular abnormalities in the KRT8 reporter hESC cell line, as evidenced by the sustained expression of pluripotent factors and a transcriptome that closely resembled that of wild-type hESCs (Figures 1C, S1D, and S1E). To verify the utility of this reporter system, we induced differentiation of the reporter hESC into SE cells. Notably, we observed ZsGreen expression, manifested as elongated chains and intricate filamentous networks spreading throughout the cytoplasm, and closely mirrored the pattern of endogenous KRT8 during SE differentiation (Figure 1C). These results demonstrated that the KRT8 reporter hESC cell line was successfully constructed, which enables us to better characterize and monitor the SE differentiation process.

Given that the KRT8 reporter hESC cell line provides temporal resolution and comparable quantitative data on KRT8 levels in response to specific signaling cues or TF

reporter cassette at the intended position, and PCR analysis of wild-type (WT) and reporter knockin (KI) hESCs, confirming successful genome editing.

(C) Images showing ZsGreen expression driven by the endogenous KRT8 promoter (KRT8-ZsGreen) alongside immunostaining for NANOG, KRT8, and TP63 in KRT8 reporter hESCs on D0, D3, and D7. The white box highlights a representative magnified area. Scale bar, 100 μm.

(D) Heatmap displaying the expression levels of candidate TFs that exhibited a remarkably elevated abundance in cells during the SE initiation stage.

(E) Images of the KRT8-ZsGreen in the reporter hESCs upon candidate TF gene knockdown on D3. Scale bar, 100 μm.

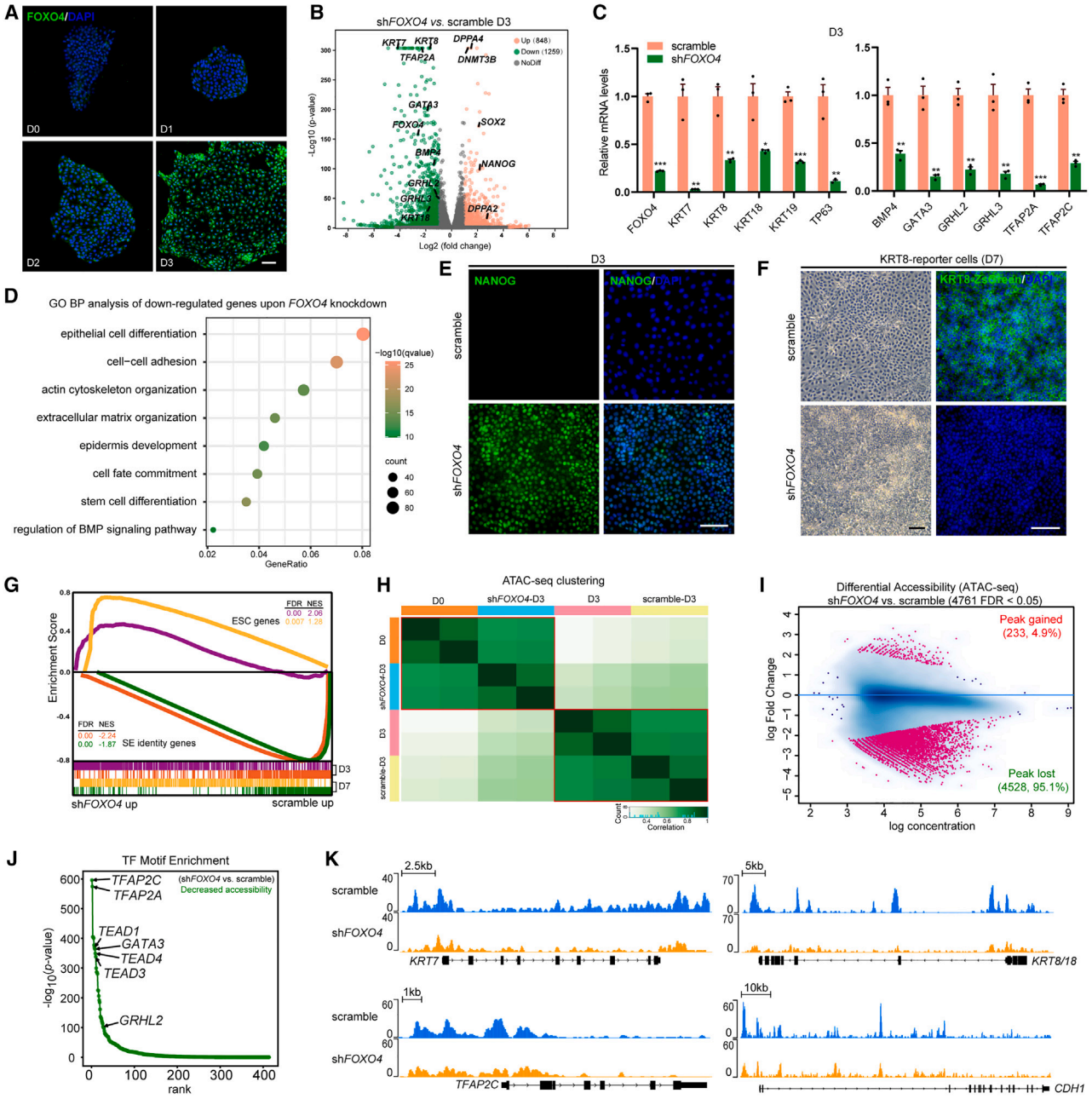

Figure 2. FOXO4 is required for SE commitment

(A) Immunostaining for FOXO4 in hESCs and differentiated cells on D1, D2, and D3. Scale bar, 100 μm.

(B) Volcano map of DEGs of sh*FOXO4*- versus scrambled shRNA-treated cells on D3. The significant DEGs (fold change ≥ 2 and *q* value < 0.05) are highlighted in orange (up-regulated genes) or green (down-regulated genes).

(C) qRT-PCR analysis for expression levels of representative genes of SE hallmark and regulators in scrambled shRNA- and sh*FOXO4*-treated cells on D3. qRT-PCR values were normalized to the values in scrambled shRNA group. Values are shown as means ± SD ($n = 3$ independent experiments; $^{**}p < 0.01$; $^{***}p < 0.001$ t test).

(D) GO (biological process) analysis of the down-regulated genes upon *FOXO4* knockdown.

(E) Immunostaining for NANOG in scrambled shRNA- and sh*FOXO4*-treated cells on D3. Scale bar, 100 μm.

(F) Images of phase contrast (left) and KRT8-ZsGreen (right) of scrambled shRNA- and sh*FOXO4*-treated KRT8 reporter cells on D7. Scale bar, 100 μm.

(legend continued on next page)

activation, which are crucial for understanding differentiation dynamics and precisely identifying key regulatory events, we subsequently utilized the reporter cell line to identify dominant TFs that function primarily at the SE initiation stage. Initially, we compared the transcriptomes of hESCs and SE-initiating cells (D3) and identified the top 20 TFs that were highly expressed at the SE initiation stage (Figure 1D). Notably, several of these TFs, including *TFAP2C*, *GRHL2*, and *GRHL3*, have been previously recognized as key regulators of SE development (Collier et al., 2023; Huang et al., 2022; Li et al., 2019), suggesting the potential influence of these candidate TFs on SE development. To identify SE lineage-specific regulators, we excluded *ID1*, *ID2*, *ID3*, *SFPQ*, *ARID3A*, and *REPIN1*, which exhibited considerable expression levels in hESC (Figure S1F). Ultimately, we selected a set of 11 TFs that, akin to the well-established key regulators *TFAP2A*, *TFAP2C*, and *GRHL3*, were specifically highly expressed at the SE initiation stage for further investigation (Figures 1D, S1F, and S1G). After knocking down candidate TFs in KRT8 reporter hESCs followed by SE differentiation, we assessed their functional significance by monitoring KRT8 dynamics visualized via ZsGreen. Notably, among the panel of candidate genes investigated, the depletion of *FOXO4*, *SP6*, *ELF3*, *MSX2*, and *ZFP36L2* led to a remarkably diminished expression of ZsGreen during SE initiation, indicating the perturbed expression patterns of KRT8 (Figures 1E, S1H, and S1I). Furthermore, upon knockdown of these genes, the differentiated cells exhibited aberrant cell morphologies and failed to undergo the characteristic epithelial-like transition (Figure S1J). By comparing the transcriptomes of mouse SE at embryonic day 9 and keratinocytes at embryonic day 13, we found that *Foxo4*, *Sp6*, and *Msx2* were highly expressed in SE (Figure S1K), further suggesting their involvement in regulating SE development (Fan et al., 2018).

FOXO4 mediates SE commitment by orchestrating the transcriptome and chromatin accessibility landscape

Given that among the candidate TFs, knockdown of *FOXO4* showed the most pronounced suppression on KRT8-ZsGreen expression during SE initiation, we therefore selected *FOXO4* to further investigate its role in SE commitment. By examining the expression dynamics of FOXO4 across the progression of SE initiation, we observed that its expression gradually increased during the first 2 days of differentiation and then dramatically elevated on the third day of differentiation (Figures 2A and S2A). We initially investigated the impact of FOXO4 on hESCs prior to differentiation and found that the clonal growth and maintenance of pluripotency in hESCs remained unaffected after *FOXO4* depletion (Figures S2B and S2C). To further explore the role of FOXO4 during SE initiation, we investigated the transcriptional alterations in *FOXO4* knockdown and control SE-initiating cells. We found that the knockdown of *FOXO*4 resulted in significant disruption of the transcriptome during the SE initiation stage, with a set of 848 up-regulated and 1,259 down-regulated genes being identified (Figure 2B). Particularly, among the differentially expressed genes (DEGs), there was a notable suppression of SE hallmark genes such as *KRT7*, *KRT8*, *KRT18*, *KRT19*, and *TP63*, as well as critical regulators of SE differentiation, including *BMP4*, *GATA3*, *GRHL2*, *GRHL3*, *TFAP2A*, and *TFAP2C* (Figure 2C). Moreover, Gene Ontology (GO) enrichment analysis revealed a robust correlation between the genes that were down-regulated in *FOXO4*-knockdown cells and crucial biological processes, encompassing epithelial cell differentiation, cell fate commitment, and regulation of BMP signaling pathway (Figure 2D). Furthermore, the pluripotency factors, namely *NANOG*, *SOX2*, *DPPA2*, *DPPA4*, and *DNMT3B*, were up-regulated upon *FOXO4* knockdown (Figures 2B and 2E). We wondered if the deficiency of *FOXO4* likewise impedes the maturation of SE development. Remarkably, the inability of *FOXO4*-depleted cells to attain terminal maturation was evident from the diminished expression of KRT8-ZsGreen, aberrant morphological features of SE cells, and a suppressed SE transcriptome during the maturation phase (Figures 2F and S2D). Gene set enrichment analysis (GSEA) likewise revealed a striking similarity between the SE identity gene set and the genes down-regulated upon *FOXO4* depletion during both the initiation and maturation stages of SE development (Figure 2G). Conversely, genes preferentially expressed in hESCs mirrored the up-regulated genes observed in the context of *FOXO4* knockdown (Figure 2G).

To elucidate the mechanisms that govern FOXO4-mediated SE commitment, we employed an approach utilizing

(G) GSEA for embryonic stem cell (ESC) and SE identity genes in the gene expression matrix of sh*FOXO4*- versus scrambled shRNA-treated cells on D3 and D7. The used ESC gene set (Assou et al., 2007) and SE identity gene set (Huang et al., 2022) are from published research.
(H) Hierarchical clustering of the indicated ATAC-seq profiles. Pearson correlation coefficients between each group are presented.
(I) Scatterplot of differential ATAC-seq peaks in sh*FOXO4*- versus scrambled shRNA-treated cells on D3. Sites identified as differential peaks with significance (FDR < 0.05) are shown in red.
(J) TF motif enrichment in the regions with decreased accessibility in sh*FOXO4*- versus scrambled shRNA-treated cells on D3.
(K) Genome browser tracks comparing ATAC-seq signal across *KRT7*, *KRT8/18*, *TFAP2C*, and *CDH1* loci of scrambled shRNA- or sh*FOXO4*-treated cells on D3.

an assay for transposase-accessible chromatin (ATAC) coupled with high-throughput sequencing (ATAC-seq). Notably, the global chromatin accessibility landscape underwent profound changes upon *FOXO4* depletion during the SE initiation stage, resulting in a chromatin accessibility state that was highly similar to that of hESCs (Figure 2H). Significantly, substantial differential chromatin regions (95.1%) showed decreased accessibility (Figure 2I), which, upon TF motif enrichment analysis, revealed an enrichment of motifs for pivotal SE regulators, including TFAP2A, TFAP2C, GATA3, and GRHL2 (Figure 2J). Furthermore, we found that the target genes of decreased ATAC peaks were remarkably down-regulated upon *FOXO4* depletion (Figure S2E), while the chromatin loci of the down-regulated genes exhibited an evident closed state (Figure S2F), revealing the strong correlation between the significantly suppressed SE transcriptome and the decreased chromatin accessibility landscape upon *FOXO4* depletion. Specifically, the genomic loci of crucial SE genes *KRT7*, *KRT8/18*, *TFAP2C*, and *CDH1* showed a diminished ATAC-seq peak upon *FOXO4* knockdown (Figure 2K). Collectively, our findings underscore the pivotal role of FOXO4 in modulating SE commitment.

FOXO4 regulates SE commitment by modulating H3K4me3 deposition

To further dissect the regulatory mechanisms underlying FOXO4-mediated SE lineage commitment, we employed chromatin immunoprecipitation with sequencing (ChIP-seq). Distribution analysis revealed that the FOXO4-binding sites were predominantly located in the promoter regions that are in close proximity to the transcription start site of its target genes (Figures 3A and 3B). Integrating transcriptome data, we revealed that 57% of DEGs of *FOXO4*-depleted cells, including SE marker genes *KRT8*, *KRT19*, *BMP4*, *CDH1*, *TFAP2C*, *GRHL2*, *GRHL3*, and *GATA3*, were bound by FOXO4 (Figure 3C). To further explore the epigenetic landscape across FOXO4-binding sites, we integrated the epigenetic map to gain deeper insights into the FOXO4 regulatory mechanism. The integrated analysis showed that the H3K4me3 modification, a mark of promoter regions, exhibits significant enrichment across the FOXO4-bound center, in contrast to the H3K4me1 modification, emphasizing that FOXO4 regulates gene expression mainly through binding promoters (Figures 3D and 3E). We subsequently analyzed the alteration of the global H3K4me3 deposition pattern under *FOXO4* disruption. Notably, genetic ablation of *FOXO4* resulted in profound changes in the H3K4me3 landscape, with the identification of 13,414 differential peaks, evenly distributed between increases and decreases (Figure 3F). The increased H3K4me3 peaks that harbor direct FOXO4-binding sites specifically target the up-regulated genes following *FOXO4* ablation, including pluripotency factors like *DPPA4*, *DNMT3B*, *SOX2*, and *NANOG*, while those diminished peaks correspond to the SE regulators (*TFAP2C*, *GRHL2*, *GRHL3*, and *GATA3*) and the previously identified candidate TFs (*SP6*, *MSX2*, *SMAD6*, and *EPAS1*) (Figure 3G). Specifically, FOXO4 bound to the promoters of core pluripotency regulators *NANOG* and *SOX2*, suppressing their expression by eliminating H3K4me3 modification during SE differentiation (Figure 3H). Conversely, the promoter regions of key SE regulators *TFAP2C* and *GRHL3* were occupied by FOXO4, which promoted the establishment of H3K4me3 deposition across their genomic loci, thereby regulating their gene expression (Figure 3H). Collectively, these findings reveal that FOXO4 orchestrates SE commitment via modulating the deposition of H3K4me3.

SP6 serves as a key downstream regulator of FOXO4

As a direct regulatory target of FOXO4, SP6 likewise exhibits notable perturbations in the differentiation process of reporter hESCs toward SE following its knockdown (Figures 1E, 4A, and S1J), thereby strongly attracting our interest. To further illuminate the regulatory relationship between FOXO4 and SP6, we individually silenced FOXO4 and SP6 and assessed their effects on the expression of each other. We found that the depletion of *FOXO4* significantly suppressed *SP6* expression, whereas the knockdown of *SP6* did not affect *FOXO4* expression (Figures 4B and 4C), suggesting that SP6 acts as a downstream regulator of FOXO4. Depletion of *SP6* did not compromise the clone formation or the pluripotency maintenance of hESCs (Figure S3A). We next sought to further elucidate the role of SP6 in governing SE fate determination and initially examined its expression level during SE initiation. We observed that SP6 is absent in hESCs, with a marked elevation in abundance observed as the cells progress toward the initiation stage of SE (Figure 4D). Through functional validation, we found that *SP6*-depleted cells exhibit an inability to commit to the SE lineage, characterized by aberrant expression patterns of KRT8 and TP63, along with the absence of characteristic epithelial morphological features during the maturation stage (Figure 4E), similar to the failure of *FOXO4*-deficient cells to attain SE commitment. Moreover, our transcriptome profiling of *SP6*-depleted cells unveiled a profound suppression of hallmark genes (including *KRT7*, *KRT8*, *KRT18*, *KRT19*, *TP63*, *DSP*, and *COL3A1*) and key regulators (*BMP4*, *GATA3*, *GRHL2*, *GRHL3*, *TFAP2A*, and *TFAP2C*) of SE, spanning both the initiation and maturation stages (Figures 4F, S3B, and S3C). Notably, GSEA confirmed a robust correlation between these down-regulated genes and SE identity genes (Figure 4G). GO analysis revealed that genes up-regulated upon *SP6* depletion were associated with biological processes fundamental to

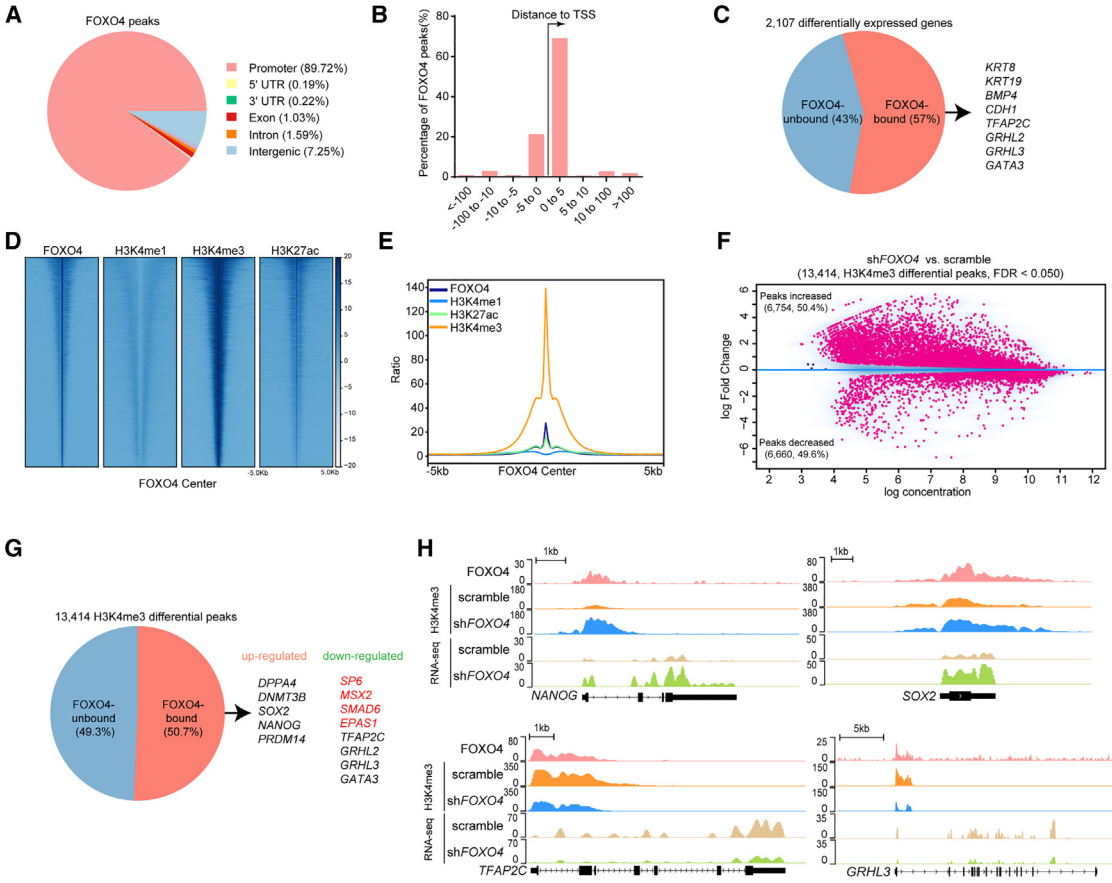

Figure 3. FOXO4 modulates H3K4me3 deposition to regulate the expression of pluripotency genes and SE genes

(A) Pie chart of FOXO4 peak distribution in differentiated cells on D3.

(B) Histogram showing the distribution of the distance between FOXO4 peaks and transcription start sites.

(C) Pie chart showing the percentage of the DEGs of sh*FOXO4*- versus scrambled shRNA-treated cells on D3 with or without FOXO4 binding.

(D) Heatmaps of H3K4me1, H3K4me3, and H3K27ac signals at the center of FOXO4 peaks in differentiated cells on D3.

(E) Metaplots of average H3K4me1, H3K4me3, and H3K27ac density across the center of FOXO4 peaks in differentiated cells on D3.

(F) Scatterplot of differential H3K4me3 peaks in sh*FOXO4*- versus scrambled shRNA-treated cells on D3. Sites identified as differential peaks with significance (FDR < 0.05) are shown in red.

(G) Pie chart showing the percentage of the differential H3K4me3 peaks upon *FOXO4* knockdown with or without FOXO4 binding. The representative up-regulated and down-regulated genes upon *FOXO4* knockdown associated with FOXO4-bound differential H3K4me3 peaks are shown.

(H) Genome browser view of FOXO4, H3K4me3, and RNA-seq signal across *NANOG*, *SOX2*, *TFAP2C*, and *GRHL3* loci.

embryonic patterning and stem cell maintenance (Figure 4H). Conversely, the down-regulated genes were linked to developmental processes including cell fate commitment, stem cell differentiation, and response to BMP (Figure 4H). Remarkably, the transcriptome profiles of *SP6*- and *FOXO4*-deficient cells exhibited a striking resemblance (Figure S3D), with GSEA further revealing that the genes suppressed upon *SP6* knockdown were significantly correlated with those down-regulated following *FOXO4* disruption (Figure 4I). Collectively, these results indicate the indispensable function of SP6, positioned downstream of FOXO4, in orchestrating the SE differentiation.

SP6 depletion impairs H3K27ac deposition across SE lineage-specific super-enhancers

We subsequently performed ATAC-seq to attain a deeper understanding of the underlying regulatory mechanisms of SP6. Notably, the global chromatin accessibility landscape of *SP6*-depleted cells significantly disrupted, displaying a remarkable resemblance to that observed in *FOXO4*-deficient cells (Figure S4A). By performing differential accessibility analysis, we identified substantial (6,219) differential ATAC peaks upon *SP6* depletion, with an overwhelming majority (97.1%) of these peaks exhibiting a marked decrease in accessibility (Figure S4B). Furthermore,

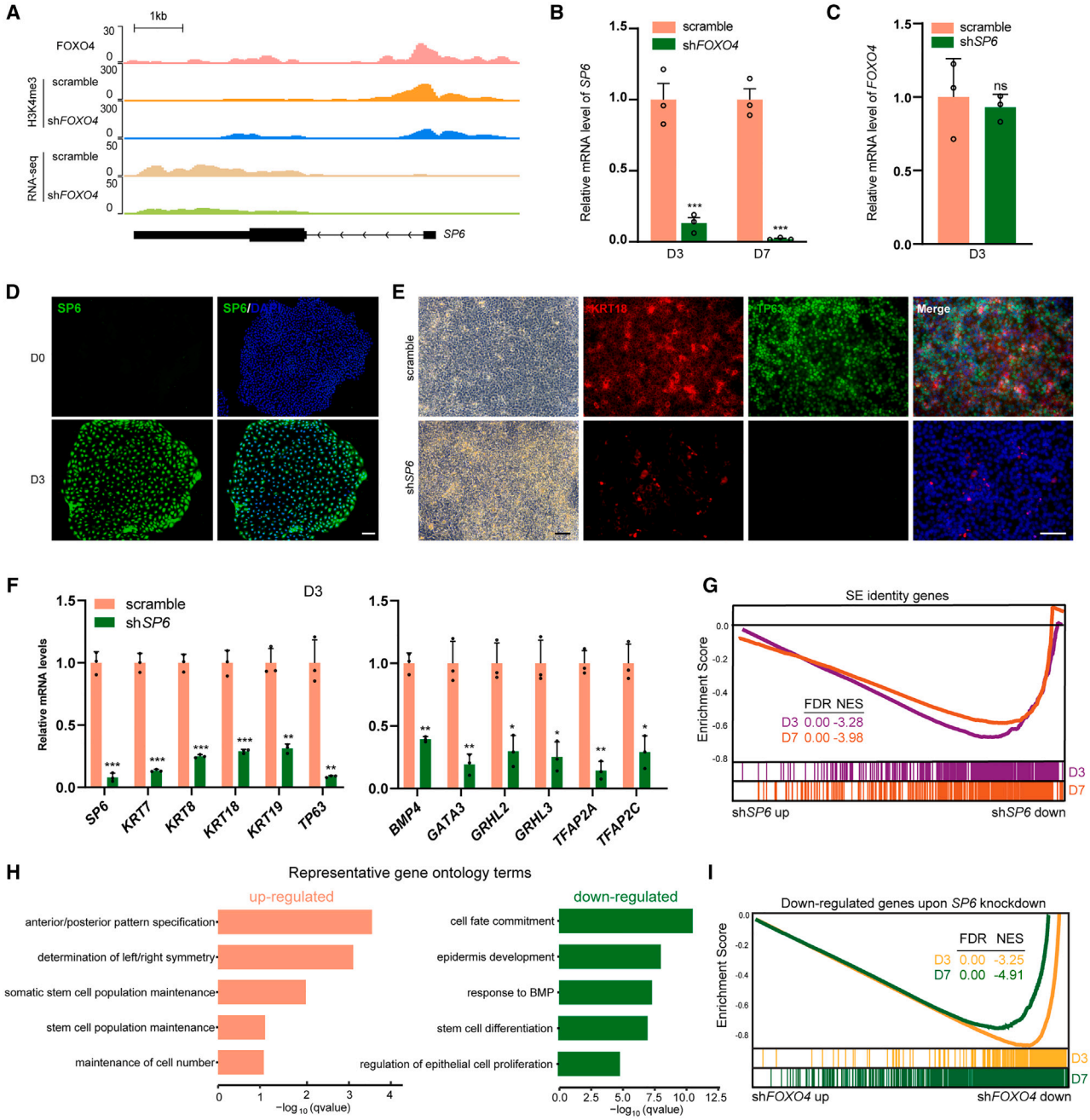

Figure 4. *SP6* depletion impairs SE commitment

(A) Genome browser view of FOXO4, H3K4me3, and RNA-seq signal across *SP6* loci.

(B) qRT-PCR analysis for expression level of *SP6* in scrambled shRNA- and sh*FOXO4*-treated cells on D3 and D7. qRT-PCR values were normalized to the values in scrambled shRNA group. Values are shown as means ± SD ($n = 3$ independent experiments; ***$p < 0.001$ t test).

(C) qRT-PCR analysis for expression level of *FOXO4* in scrambled shRNA- and sh*SP6*-treated differentiated cells on D3. qRT-PCR values were normalized to the values in scrambled shRNA group. Values are shown as means ± SD ($n = 3$ independent experiments; ns means not statistically significant, t test).

(D) Immunostaining for SP6 in hESCs and differentiated cells on D3. Scale bar, 100 μm.

(E) Phase-contrast images and immunostaining for KRT18 and TP63 in scrambled shRNA- and sh*SP6*-treated differentiated cells on D7. Scale bar, 100 μm.

(legend continued on next page)

peaks decreasing in accessibility following *SP6* knockdown were enriched for the motif of SE regulators (TFAP2A, TFAP2C, GATA3, and GRHL2), and the peaks increasing in accessibility were enriched for pluripotent factor motifs (Figure S4C).

We then employed ChIP-seq to identify the genome-wide binding profiles of SP6. Distribution analysis revealed that SP6 exhibits a predominant occupancy within distal intergenic regions, positioned at a distance from transcription start sites (Figures 5A and 5B). Notably, the SP6-binding sites were enriched with motifs of key SE regulators, including GATA3, TFAP2A, TFAP2C, and GRHL2, suggesting a pivotal modulatory role for SP6 within SE regulatory networks (Figure S4D). When integrated with the transcriptome data under conditions of *SP6* disruption, we identified a substantial fraction (66.7%) of DEGs that harbor SP6-binding sites, including critical SE genes such as *KRT8*, *GATA3*, *GRHL2*, *GRHL3*, *TFAP2C*, and *BMP4*, as well as *SP6* itself (Figure 5C). These SP6-targeted DEGs were significantly enriched in biological processes fundamental to cell differentiation and fate commitment (Figure S4E). We further investigate the coordination between FOXO4 and SP6 in SE fate determination by integrating SP6 and FOXO4 ChIP-seq and RNA sequencing (RNA-seq) analyses. We found that although the majority of peaks between FOXO4 and SP6 do not overlap (Figure S4F), their common target genes, including key SE genes, *BMP4*, *KRT8*, *KRT19*, *TFAP2C*, *GRHL2*, *GRHL3*, and *MSX2*, were enriched in GO terms related to pan-epithelial development processes (Figures S4G and S4H), suggesting a synergistic regulatory role of FOXO4 and SP6 in modulating SE commitment.

To further dissect the epigenetic landscape across SP6-binding sites, we integrated the SP6 ChIP-seq data with the epigenetic map for comprehensive analysis. The results revealed a significant enrichment of active histone marks, specifically H3K4me1, H3K4me3, and H3K27ac, across SP6-bound centers (Figure 5D). Notably, the SP6-binding sites can be categorized into two distinct groups based on their epigenetic modification profiles: a minor group located specifically on promoters and enriched with the H3K4me3 mark and a major group predominantly residing on enhancers marked by H3K4me1 (Figure 5D). Given the extensive binding of SP6 to active enhancer regions, we investigated whether SP6 modulates SE differentiation processes by regulating lineage-specific super-enhancers, a distinctive class of genomic elements, which play a pivotal role in lineage commitment and the establishment of cellular identity (Adam et al., 2015; Hnisz et al., 2013; Whyte et al., 2013). We identified a set of 1,111 super-enhancers at the SE initiation stage (Figure 5E), with a notable direct correspondence between these super-enhancers and core SE genes such as *GRHL2*, *GRHL3*, *TFAP2C*, *BMP4*, *KRT8*, *KRT18*, and *MSX2* (Figure 5E). GO analysis further emphasized the significant enrichment of genes associated with these super-enhancers in biological processes critical for SE development, underscoring the significance of the identified super-enhancers as key indicators of SE identity (Figure S4I). Importantly, we found that SP6 bound to the majority of SE lineage super-enhancers (69.2%) (Figure 5F). Furthermore, GO enrichment analysis revealed that these super-enhancer genes regulated by SP6 were implicated in vital epithelium developmental processes (Figure 5G). We further compared the binding maps of H3K27ac in scrambled short hairpin (sh) RNA- and sh*SP6*-treated differentiated cells to determine whether SP6 mediated the establishment of the SE lineage-specific super-enhancer landscape. Notably, following *SP6* depletion, we observed a substantial reduction in H3K27ac signals across SP6-bound super-enhancers (Figures 5H and 5I), and these super-enhancer regulated genes exhibited marked disruption at the SE initiation stage (Figure 5J). Specifically, SP6 occupied super-enhancers at the genomic loci of *KRT8/18*, *TFAP2C*, and *MSX2*, modulating chromatin accessibility and the epigenetic landscape around these regions. In the absence of *SP6*, the deposition of H3K27ac across these super-enhancer loci was significantly diminished, resulting in disrupted gene expression (Figure 5K). Collectively, these results suggest that SP6 modulates SE lineage-specific genes via orchestrating SE-specific super-enhancers.

DISCUSSION

SE lineage-specific regulators exert their robust function in controlling SE lineage commitment, and their dysfunction or mutation can lead to severe developmental abnormalities or disease manifestations. Tremendous efforts have been directed toward identifying lineage-determining TFs

(F) qRT-PCR analysis for expression levels of representative genes of SE hallmark and regulators in scrambled shRNA- and sh*SP6*-treated differentiated cells on D3. qRT-PCR values were normalized to the values in scrambled shRNA group. Values are shown as means ± SD ($n = 3$ independent experiments; $^{*}p < 0.05$; $^{**}p < 0.01$; $^{***}p < 0.001$ t test).
(G) GSEA for SE identity genes in the gene expression matrix of sh*SP6*- versus scrambled shRNA-treated differentiated cells on D3 and D7. The used SE identity gene set is from published research (Huang et al., 2022).
(H) GO (biological process) analysis of the up-regulated (left) and down-regulated genes (right) upon *SP6* knockdown.
(I) GSEA for down-regulated genes upon *SP6* knockdown in the gene expression matrix of sh*FOXO4*- versus scrambled shRNA-treated differentiated cells on D3 and D7.

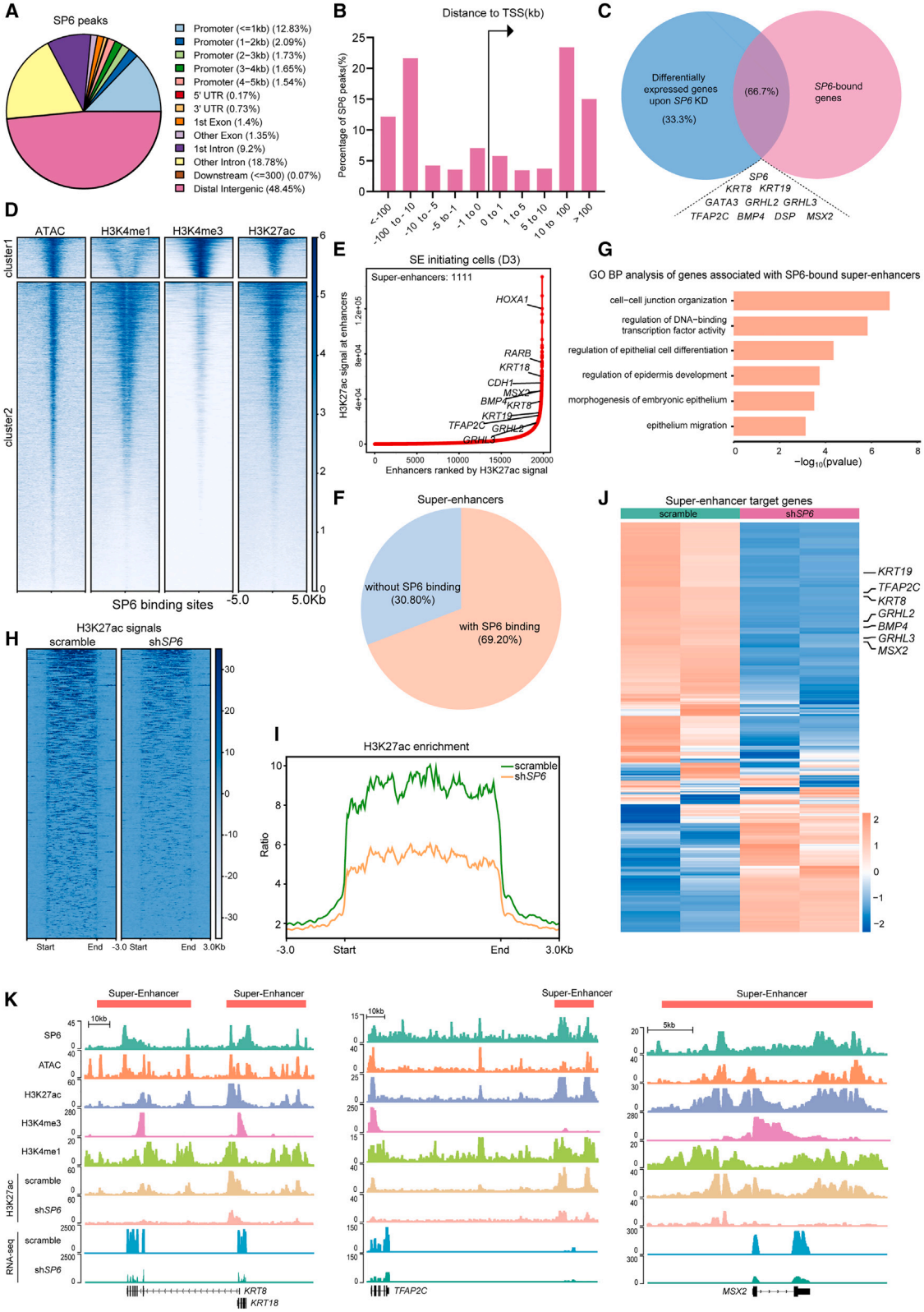

(legend on next page)

and dissecting their regulatory networks during cell fate decisions. By employing the KRT8 reporter system, we identified FOXO4 and SP6 as SE fate-essential TFs and formed a regulatory axis controlling SE commitment. Furthermore, we wire the chromatin reorganization, epigenetic landscape establishment, and genetic regulation under FOXO4-SP6 axis-mediated SE commitment (Figure 6).

It has been reported that the expression of FOXO4 decreases during the differentiation of hESCs into neural, trophoblast, and fibroblast lineages, and *FOXO4* knockdown impairs neural lineage commitment without affecting the differentiation of trophoblasts and fibroblasts (Vilchez et al., 2012, 2013). Here, we observed that the expression pattern of FOXO4 during SE fate determination was notably different, with low levels in hESCs that rapidly increase during the initiation phase of SE. Functional assays demonstrated that FOXO4 is a novel and essential regulator of SE, crucial for SE commitment. These results indicate that FOXO4 plays distinct roles in the determination of different lineage fates.

Mechanistically, we found that FOXO4 mediates SE commitment through a mechanism involving the activation of H3K4me3 modification at the promoters of SE lineage-specific genes, thereby positively regulating the transcription of their target genes. This aligns with the previous reports that FOXO family members exert regulatory function by binding to the promoters of their target genes and consequently mediate their transcription (Link, 2019). It has been shown that H3K4 methyltransferases of the SET1/COMPASS family, such as MLL1/2, SETD1A/B, WDR5, DPY30, and CFP1, are responsible for regulating H3K4me3 modifications during transcriptional co-regulation (Ang et al., 2011; Clouaire et al., 2012; Denissov et al., 2014; Jiang et al., 2011; Zhang et al., 2025). Therefore, exploring the relationship between H3K4 methyltransferases and FOXO4 could facilitate a comprehensive understanding of the regulatory mechanisms of FOXO4 in development.

The common target genes of FOXO4 and SP6 were enriched in GO terms associated with pan-epithelial developmental processes, suggesting that FOXO4 and SP6 synergistically regulate SE lineage-specific genes. However, their binding maps demonstrated the distinct DNA-binding patterns. The distinction between FOXO4 and SP6 prompted us to postulate a mechanism by which FOXO4 coordinates with SP6 to mediate SE gene expression through long-range enhancer-promoter interactions. Therefore, further investigation into the three-dimensional enhancer-promoter interactions mediated by FOXO4 and SP6 will be of particular interest in future studies.

A set of crucial developmental TFs known to be essential for SE cell fate determination, including TFAP2C, GRHL2, GRHL3, and MSX2, were identified as target genes of SE lineage-specific super-enhancers. We identified SP6 as a novel regulator of SE initiation, binding to a substantial proportion of SE lineage-specific super-enhancers and modulating the deposition of H3K27ac, thereby regulating the transcription of target genes, which is similar to the previous study that SP6 exerts its regulatory function during trophoblast development by modulating the H3K27ac landscape at targeted regulatory elements (Chen et al., 2024).

The reporter line facilitates the identification of distinct cell states during cell fate transition, enabling the sorting and enrichment of target cells at various developmental stages, and serves as powerful tool to investigate potential crucial regulators involved in lineage commitment. Utilizing the reporter line, we also found that within the candidate TFs for key SE regulators, *ELF3* and *ZFP36L2* likewise showed disruption of KRT8 expression upon depletion. Thus, it is worth further exploring their contribution to SE commitment and elucidating the intricate regulatory hierarchy that interconnects them with the FOXO4-SP6 axis in future studies.

Collectively, our findings offer detailed insights into the molecular mechanisms underlying SE development,

Figure 5. SP6 orchestrates SE commitment via lineage-specific super-enhancers

(A) Pie chart of SP6 peak distribution in differentiated cells on D3.
(B) Histogram showing the distribution of the distance between SP6 peaks and transcription start sites.
(C) Venn diagram showing the overlap among SP6 target genes and DEGs of sh*SP6*- versus scrambled shRNA-treated cells on D3.
(D) Heatmaps of ATAC-seq, H3K4me1, H3K4me3, and H3K27ac signals at the center of SP6 peaks in differentiated cells on D3.
(E) Ranked enhancer plots defined by H3K27ac. Enhancers above the inflection point of the curve show exceptionally robust H3K27ac signals and are defined as super-enhancers. The exhibited genes are super-enhancer-associated genes that are critical for SE identity.
(F) Pie chart showing the percentage of the identified super-enhancers with or without SP6 binding.
(G) GO (biological process) analysis of the genes associated with super-enhancers with SP6 binding.
(H) Heatmaps of H3K27ac signals across SP6-bound super-enhancers in scrambled shRNA- and sh*SP6*-treated cells on D3.
(I) Metaplots of average H3K27ac density across SP6-bound super-enhancers in scrambled shRNA- and sh*SP6*-treated cells on D3.
(J) Heatmap of expression levels of SP6-bound super-enhancer-associated genes in scrambled shRNA- and sh*SP6*-treated cells on D3.
(K) Genome browser view of SP6, ATAC-seq, H3K27ac, H3K4me3, H3K4me1, and RNA-seq signals across *KRT8/18*, *TFAP2C*, and *MSX2* loci. The super-enhancer regions are indicated.

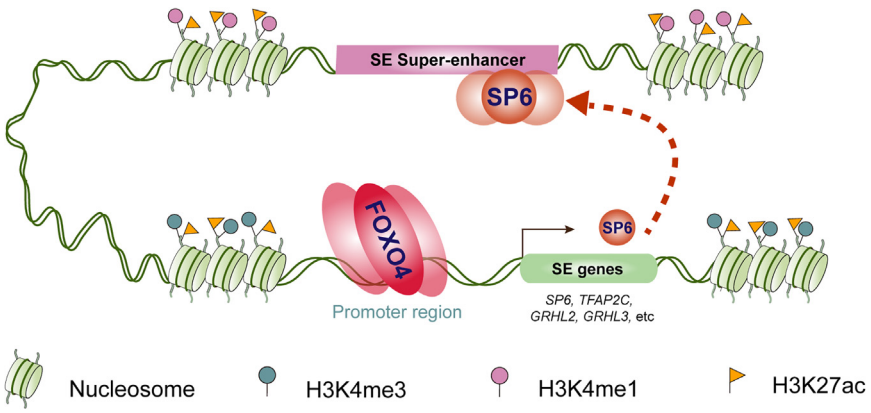

Figure 6. A proposed mechanistic model of FOXO4-SP6 axis-driven SE commitment

The graphical summary of the function and mechanism of the FOXO4-SP6 regulatory axis in SE commitment.

thereby facilitating a better understanding of TF regulatory principles during SE fate decision and the pathogenesis of ectodermal dysplasia.

METHODS

hESC culture

hESCs H1 (XY) and KRT8 reporter cell lines were cultured on hESC-qualified Matrigel (Corning)-coated plates in pluripotency growth media (mTeSR1) (STEMCELL Technologies). Cells were incubated at 37°C with 5% CO_2 and were routinely tested for mycoplasma. Cells were routinely passaged every 4–5 days using gentle cell dissociation reagent (STEMCELL Technologies).

Cell differentiation

For SE differentiation, H1 hESCs were digested into 100–200 μm diameter colonies with gentle cell dissociation reagent (STEMCELL Technologies) and treated with 1 μM RA (R&D Systems) in mTeSR1 medium for 7 days. The culture medium was replaced every 2 days. For induction of SE into keratinocytes, SE was then cultured in defined keratinocyte-SFM medium (DKSFM, Gibco) supplemented with 10 ng mL^{-1} fibroblast growth factor (FGF) (R&D Systems) and 10 ng mL^{-1} epidermal growth factor (EGF) (Millipore) for 60 days. The culture media was replaced every day. To induce terminal differentiation, derived keratinocytes were treated with 1.2 mM $CaCl_2$ in DKSFM medium for 7 days when cells reach full confluence.

Air-lifting culture system

7×10^5 derived keratinocytes were digested and seeded into 1% type I collagen-coated transwell inserts (0.4 μm polyester membrane, Corning) in 24-well culture plates. Cells were incubated for 3–5 days with both upper inserts (200 μL), and lower chambers (500 μL) were filled with DKSFM. Subsequently, the medium in upper inserts was removed, and the lower chambers remain filled with medium (200 μL) for 7–10 days. 10% neutral buffered formalin was used to fix the samples, which were then subjected to dehydration, paraffin embedding, sectioning, and immunofluorescence staining.

Generation of the KRT8 reporter cell line using the CRISPR-Cas9 system

To construct a KRT8 reporter cell line, two plasmids were designed to edit the genome of H1 hESCs. The first plasmid, a LentiCRISPRv2 vector, was engineered to carry a specific guide RNA (gRNA), designed by an online tool (http://chopchop.cbu.uib.no/), targeting the sequence proximal to the stop codon of the KRT8 gene. This plasmid expresses neomycin resistance for screening purposes. The second plasmid served as a donor, featuring a PUC57 backbone that harbors the reporter cassette along with homology arms of the KRT8 gene, ensuring precise integration, which also confers puromycin resistance. For transfection, 1×10^6 hESCs were digested into single cells using Accutase (Thermo Fisher Scientific, A1110501) and mixed with the plasmids. We then performed electroporation according to the manufacturer's instructions, utilizing a P3 Primary Cell 4D-Nucleofector X Kit (Lonza, V4XP-3024) in conjunction with a 4D-Nucleofector System (Lonza). After transfection, the cells were seeded onto 6-well plates and cultured in mTeSR1 medium supplemented with 10 μM Rho kinase inhibitor Y-27632. After an incubation period of 48 h, the cells were subjected to selection with 500 ng mL^{-1} puromycin and 150 μg mL^{-1} G418 for 2 days. The surviving cells were then expanded and digested into single cells to form clones, followed by PCR and Sanger sequencing to identify and isolate the successfully edited hESC line. The sequences of the PCR primers and KRT8-editing gRNA are listed in Tables S3 and S4, respectively.

Generating gene knockdown cell line using shRNA

Utilizing the Merck online tool, shRNAs were designed to specifically target *FOXO4*, *SP6*, *MSX2*, *ELF3*, *EPAS1*,

FOXI3, *GRHL1*, *ID4*, *SMAD6*, *ZMIZ1*, and *ZFP36L2* genes. Two distinct target-specific shRNAs were designed for each gene, and a non-targeting scrambled shRNA was used as a negative control. These shRNAs were subsequently subcloned into the PLKO.1 plasmid vector and confirmed by Sanger sequencing. To package lentiviral particles, these vectors were individually transfected into HEK293T cells along with the packaging plasmid psPAX2 and the envelope plasmid pMD2.G, using Lipofectamine 3000 (Thermo Fisher Scientific, L3000150). The lentiviral titer was assessed using a qPCR Lentivirus Titer Kit (Applied Biological Materials Inc.). For the gene knockdown experiments, hESCs were plated onto Matrigel-coated plates and infected with lentiviral particles in the presence of 8 μg mL^{-1} polybrene for 24 h, followed by selection using 2 μg mL^{-1} puromycin of 48 h. The knockdown efficiency of target genes was evaluated by real-time quantitative reverse-transcription PCR (qRT-PCR). The sequences of the shRNAs used in this study are listed in Table S4.

RNA extraction and real-time qRT-PCR

Total RNA was extracted utilizing the MolPure Cell/Tissue Total RNA Kit (Yeasen), followed by reverse transcription of 500 ng of RNA into cDNA with the PrimeScript RT Master Mix Kit (Takara), according to the respective manufacturer's guidelines. qRT-PCR was performed using iTaq Universal SYBR Green Supermix Kit (Bio-Rad) on a QuantStudio 7 Flex Real-Time PCR system (Thermo Fisher Scientific). The PCR program started with a denaturation step at 95°C for 3 min, which was subsequently followed by 40 cycles (95°C for 5 s and 60°C for 30 s). Relative mRNA levels were normalized to that of housekeeping gene *GAPDH*. The qRT-PCR primers used in this study are listed in Table S5.

Immunofluorescence analysis

After being washed twice with phosphate-buffered saline (PBS), the cells were fixed with 4% paraformaldehyde for 15 min at room temperature (RT). This was followed by permeabilization and blocking with a solution containing 3% bovine serum albumin and 0.3% Triton X-100 in PBS for 1 h at RT. Subsequently, the cells were incubated overnight with primary antibodies at 4°C. After washing three times with PBST (PBS containing 0.05% Tween 20), cells were then subjected to immunostaining with Alexa Fluor dye-conjugated secondary antibodies for 1 h at RT. 4′,6-diamidino-2-phenylindole (DAPI) was then used to stain the nuclei for 15 min at RT after three washes with PBST. The stained cells were imaged using a Leica DMi8 fluorescence microscope. The primary antibodies used for immunofluorescence in this study are as follows: anti-KRT7 (Cell Signaling, 4465S; 1:500), anti-KRT8 (Invitrogen, MA514428; 1:500), anti-NANOG (GeneTex, GTX100863; 1:500), anti-TP63 (Cell Signaling, 67825S; 1:500), anti-KRT14 (Invitrogen, MA5-11599; 1:500), anti-KRT10 (Invitrogen, MA1-06319; 1:1,000), anti-FOXO4 (Invitrogen, 720154; 1:500), anti-OCT4 (GeneTex, GTX101497; 1:500), anti-SP6 (Affinity Biosciences, DF9082; 1:500), and anti-KRT18 (Invitrogen, MA512104; 1:500). Secondary antibodies used included Alexa Fluor 488-conjugated anti-mouse IgG, Alexa Fluor 488-conjugated anti-rabbit IgG, Alexa Fluor 594-conjugated anti-mouse IgG, and Alexa Fluor 594-conjugated anti-rabbit IgG (Cell Signaling, 1:1,000).

RNA-seq and data analysis

The TruSeq Stranded mRNA Library Prep kit (Illumina) was used to construct the RNA-seq libraries following the manufacturer's protocol. The prepared libraries were sequenced on an Illumina NovaSeq 6000 platform with 150 bp paired-end reads. Raw sequenced reads were quality tested and adaptor-trimmed using the trimmomatic tool (version 0.39) (Bolger et al., 2014), and then the trimmed reads were aligned to human hg19 reference genome using the STAR software (version 2.6.1) (Dobin et al., 2013). The RSEM tool (version 1.3.0) was used to quantify the gene expression levels and calculate transcripts per kilobase million values (Dewey and Bo, 2011). DEGs were identified using the DESeq2 (version 1.20.0) with a cutoff of q value ≤ 0.05 and fold change ≥ 2 (Love et al., 2014). GO biological process enrichment analysis was performed using the Clusterprofiler R package with a cutoff of q value ≤ 0.05 (Yu et al., 2012). GSEA was performed using official software from Broad institute (Subramanian et al., 2005). The RNA-seq data were obtained from two biological samples.

Public transcriptome data of mouse SE at embryonic day 9 and keratinocytes at embryonic day 13 were downloaded. These data were then assessed for quality utilizing FASTQC (version 0.11.5) (Wingett and Andrews, 2018) and subsequently trimmed of adaptor sequences with Trim Galore (version 0.5.0). The reads were aligned to the mouse mm10 reference genome by employing STAR (version 2.6.1) (Dobin et al., 2013), and their abundances were quantified using RSEM (version 1.3.0) (Dewey and Bo, 2011).

ATAC-seq assay

ATAC-seq assays were performed as described previously (Huang et al., 2022). Briefly, 60,000 cells were collected and washed with cold PBS, and then incubated in ice-cold lysis buffer (10 mM Tris-HCl [pH 7.5], 0.1% Tween 20, 0.5% IGEPAL CA-630, 3 mM $MgCl_2$, and 10 mM NaCl) for 5 min. Subsequently, nuclei were collected by centrifuging at 500 g and 4°C for 10 min and removing the supernatant. After being washed with cold PBS, nuclei were resuspended and incubated in transposase reaction mix (Vazyme Biotech, TD501) at 37°C for 30 min. The

transposed DNA fragments were purified using the MinElute PCR Purification Kit (QIAGEN). Then the ATAC-seq library construction, including end-repairing, adapter ligation, and PCR amplification, was conducted using the TruePrep DNA Library Prep Kit (Vazyme Biotech, TD501), according to the manufacturer's guidelines. The VAHTS DNA Clean Beads (Vazyme Biotech, N411-01) were used to enrich the amplified library. The ATAC-seq libraries were finally subjected to sequencing on a NovaSeq 6000 platform (Illumina). The ATAC-seq data were obtained from two biological samples.

ChIP-seq assay

1×10^7 cells cultured on 10 cm culture dishes were crosslinked with 1% formaldehyde (Thermo Fisher Scientific, 28906) at RT for 10 min, and then quenched with 0.125 M glycine (Sigma, 50046) at RT for 5 min. After washing three times with cold PBS, cells were collected, resuspended, and lysed in ice-cold sonication buffer (50 mM HEPES-NaOH [pH 7.5], 500 mM NaCl, 1 mM EDTA, 0.1% SDS, 0.1% Na-deoxycholate, and 1% Triton X-100) for 10 min. For crosslinked chromatin fragmentation, sonication was performed by a Covaris M220 focused-ultrasonicator to generate DNA fragments of 200–500 bp. Subsequently, the chromatin was incubated with primary antibodies overnight at 4°C, followed by the addition of Protein A/G Dynabeads (Invitrogen) to capture the immunocomplexes. The beads were then washed three times with sonication buffer, twice with low-salt wash buffer (10 mM Tris-HCl [pH 8.0], 1 mM EDTA, 250 mM LiCl, 0.5% NP40, and 0.5% Na-deoxycholate) and once with TE buffer (10 mM Tris-HCl, pH 8.0) subsequently. After elution from the Dynabeads and decrosslinking with elution buffer (50 mM Tris-HCl [pH 8.0], 10 mM EDTA, and 1% SDS) at 65°C for 4 h, the DNA fragments were incubated with proteinase K (Invitrogen) and RNase A (Invitrogen) at 55°C for 1 h, and then purified utilizing the MinElute PCR Purification Kit (QIAGEN). ChIP-seq libraries were prepared using the KAPA Hyper Prep Kit (Kapa Biosystems, KK8502) according to the manufacturer's instructions and were subjected to sequencing on a NovaSeq 6000 platform (Illumina) using 150 bp paired-end reads. Antibodies used for ChIP-seq in this study are as follows: H3K4me1 (Active Motif, 39297), H3K4me3 (Cell Signaling, 9751S), H3K27ac (Millipore, 07-360), FOXO4 (Invitrogen, 720154), and SP6 (Affinity Biosciences, DF9082). The ChIP-seq data were obtained from two biological samples.

ChIP-seq and ATAC-seq data analysis

The analysis of ChIP-seq and ATAC-seq data was conducted following the previously described protocol (Huang et al., 2022). Briefly, raw reads underwent quality control and adapter trimming using the trimmomatic tool (version 0.39) prior to alignment (Bolger et al., 2014). Subsequently, the trimmed reads were mapped to the human hg19 reference genome utilizing the BWA software (version 0.7.17) (Li and Durbin, 2010). PCR duplicates were then removed with the Picard tools (version 2.18.16). Peak calling for both ATAC-seq and ChIP-seq data was performed using the MACS2 (version 2.1.1) (Zhang et al., 2008). For broad histone marks (H3K4me1), peak calling incorporated options "–fix-bimodal –extsize 500 –broad –broad-cutoff 0.01." For narrow histone marks and TF ChIP-seq, the options "–call-summits –fix-bimodal –extsize 200 -q 0.001" were applied. For ATAC-seq peaks, the parameters "–nomodel –shift −100 –call-summits –extsize 200 –q 0.001" were used. Overlapping peaks between biological replicates were identified with the Homer mergePeaks program. The resulting bedGraph files from MACS2 were converted to bigwig format using the deepTools bamCoverage program for visualization in the Integrative Genomics Viewer (Ramírez et al., 2016). Average profiles and heatmaps were generated for ChIP-seq and ATAC-seq data with the deepTools (version 3.0.2) (Ramírez et al., 2016). Peak distribution analysis was conducted using the ChIPseeker package (Chen et al., 2014), while peak annotation was performed with the HOMER annotatePeaks.pl program. TF motif enrichment analysis was executed by the HOMER findMotifsGenome program. Differential ChIP-seq as well as ATAC-seq peaks were identified using the DiffBind R package, with a cutoff of false discovery rate (FDR) ≤ 0.05 (Wu et al., 2015).

Super-enhancer identification

The H3K27ac signal was used to identify and annotate super-enhancers following the default parameters of the ROSE algorithm (https://bitbucket.org/young_computation/rose) (Whyte et al., 2013).

Statistical analysis

The statistical measurements were performed utilizing GraphPad Prism (version 8.0). To assess the statistical significance between two groups, an unpaired, two-tailed Student's t test was employed. The error bars depicted in the graphs were computed using GraphPad Prism (version 8.0), and the data are presented as the mean values with standard deviations (means ± SD). In all performed experiments, the *n* value represents the number of independently conducted experiments.

RESOURCE AVAILABILITY

Lead contact

Further information and requests for resources and reagents should be directed to and will be fulfilled by the lead contact, Hong Ouyang (Ouyhong3@mail.sysu.edu.cn).

Materials availability

All the materials generated and used in this study will be available upon reasonable request.

Data and code availability

ATAC-seq, ChIP-seq, and RNA-seq data have been deposited in the Gene Expression Omnibus (GEO) database. The accession number for the ATAC-seq data presented in this paper is GEO: GSE280745; the accession number for the ChIP-seq data is GEO: GSE280746; and the accession number for the RNA-seq data is GEO: GSE280747. The mouse RNA-seq data used in this paper were downloaded from the GEO under the accession number GSE97213. Other relevant data are available from the corresponding author upon reasonable request.

ACKNOWLEDGMENTS

This work was supported by National Natural Science Foundation of China (no. 82271043), National Natural Youth Science Foundation of China (no. 32400597), Natural Science Foundation of Guangdong Province (no. 2023A1515012719), and China Postdoctoral Science Foundation (no. 2023M734023). We would like to thank Professor Nan Cao for sharing H1 human embryonic stem cells.

AUTHOR CONTRIBUTIONS

H.O. conceived and guided this project and contributed to the writing. Jiafeng Liu and H.H. designed and performed the experiments, conducted bioinformatics analyses, and wrote the manuscript. F.A. was responsible for performing cellular and molecular biology experiments. S.W., H.G., B.W., and Z.H. contributed to the cellular experiments. J.T., Z.L., Y.F., Jinpeng Liu, H.Y., and Y.D. participated in molecular biology experiments. K.M., Y.H., M.L., L.W., and Z.M. provided comments and assisted with the experiments.

DECLARATION OF INTERESTS

The authors declare no competing interests.

SUPPLEMENTAL INFORMATION

Supplemental information can be found online at https://doi.org/10.1016/j.stemcr.2025.102445.

Received: November 1, 2024
Revised: February 10, 2025
Accepted: February 11, 2025
Published: March 13, 2025

REFERENCES

Adam, R.C., Yang, H., Rockowitz, S., Larsen, S.B., Nikolova, M., Oristian, D.S., Polak, L., Kadaja, M., Asare, A., Zheng, D., and Fuchs, E. (2015). Pioneer factors govern super-enhancer dynamics in stem cell plasticity and lineage choice. Nature *521*, 366–370. https://doi.org/10.1038/nature14289.

Ang, Y.S., Tsai, S.Y., Lee, D.F., Monk, J., Su, J., Ratnakumar, K., Ding, J., Ge, Y., Darr, H., Chang, B., et al. (2011). Wdr5 mediates self-renewal and reprogramming via the embryonic stem cell core transcriptional network. Cell *145*, 183–197. https://doi.org/10.1016/j.cell.2011.03.003.

Assou, S., Le Carrour, T., Tondeur, S., Ström, S., Gabelle, A., Marty, S., Nadal, L., Pantesco, V., Réme, T., Hugnot, J.P., et al. (2007). A meta-analysis of human embryonic stem cells transcriptome integrated into a web-based expression atlas. Stem Cells *25*, 961–973. https://doi.org/10.1634/stemcells.2006-0352.

Biggs, L.C., and Mikkola, M.L. (2014). Early inductive events in ectodermal appendage morphogenesis. Semin. Cell Dev. Biol. *25–26*, 11–21. https://doi.org/10.1016/j.semcdb.2014.01.007.

Bolger, A.M., Lohse, M., and Usadel, B. (2014). Trimmomatic: a flexible trimmer for Illumina sequence data. Bioinformatics *30*, 2114–2120. https://doi.org/10.1093/bioinformatics/btu170.

Carpenter, A.C., Smith, A.N., Wagner, H., Cohen-Tayar, Y., Rao, S., Wallace, V., Ashery-Padan, R., and Lang, R.A. (2015). Wnt ligands from the embryonic surface ectoderm regulate 'bimetallic strip' optic cup morphogenesis in mouse. Development *142*, 972–982. https://doi.org/10.1242/dev.120022.

Chen, T.W., Li, H.P., Lee, C.C., Gan, R.C., Huang, P.J., Wu, T.H., Lee, C.Y., Chang, Y.F., and Tang, P. (2014). ChIPseek, a web-based analysis tool for ChIP data. BMC Genom. *15*, 539. https://doi.org/10.1186/1471-2164-15-539.

Chen, X., Hu, J., Wang, Y., Lee, Y., Zhao, X., Lu, H., Zhu, G., Wang, H., Jiang, Y., Liu, F., et al. (2022). The FoxO4/DKK3 axis represses IFN-γ expression by Th1 cells and limits antimicrobial immunity. J. Clin. Investig. *132*, e147566. https://doi.org/10.1172/jci147566.

Chen, Y., Ye, X., Zhong, Y., Kang, X., Tang, Y., Zhu, H., Pang, C., Ning, S., Liang, S., Zhang, F., et al. (2024). SP6 controls human cytotrophoblast fate decisions and trophoblast stem cell establishment by targeting MSX2 regulatory elements. Dev. Cell *59*, 1506–1522.e11. https://doi.org/10.1016/j.devcel.2024.03.025.

Clouaire, T., Webb, S., Skene, P., Illingworth, R., Kerr, A., Andrews, R., Lee, J.H., Skalnik, D., and Bird, A. (2012). Cfp1 integrates both CpG content and gene activity for accurate H3K4me3 deposition in embryonic stem cells. Genes Dev. *26*, 1714–1728. https://doi.org/10.1101/gad.194209.112.

Collier, A.E., Piekos, S.N., Liu, A., Pattison, J.M., Felix, F., Bailetti, A.A., Sedov, E., Gaddam, S., Zhen, H., and Oro, A.E. (2023). GRHL2 and AP2a coordinate early surface ectoderm lineage commitment during development. iScience *26*, 106125. https://doi.org/10.1016/j.isci.2023.106125.

Collomb, E., Yang, Y., Foriel, S., Cadau, S., Pearton, D.J., and Dhouailly, D. (2013). The corneal epithelium and lens develop independently from a common pool of precursors. Dev. Dyn. *242*, 401–413. https://doi.org/10.1002/dvdy.23925.

Denissov, S., Hofemeister, H., Marks, H., Kranz, A., Ciotta, G., Singh, S., Anastassiadis, K., Stunnenberg, H.G., and Stewart, A.F. (2014). Mll2 is required for H3K4 trimethylation on bivalent promoters in embryonic stem cells, whereas Mll1 is redundant. Development *141*, 526–537. https://doi.org/10.1242/dev.102681.

Dewey, C.N., and Bo, L. (2011). RSEM: accurate transcript quantification from RNA-Seq data with or without a reference genome. BMC Bioinf. *12*, 323.

Di Girolamo, N., and Park, M. (2023). Cell identity changes in ocular surface Epithelia. Prog. Retin. Eye Res. *95*, 101148. https://doi.org/10.1016/j.preteyeres.2022.101148.

Dobin, A., Davis, C.A., Schlesinger, F., Drenkow, J., Zaleski, C., Jha, S., Batut, P., Chaisson, M., and Gingeras, T.R. (2013). STAR: ultrafast universal RNA-seq aligner. Bioinformatics *29*, 15–21. https://doi.org/10.1093/bioinformatics/bts635.

Fan, X., Wang, D., Burgmaier, J.E., Teng, Y., Romano, R.A., Sinha, S., and Yi, R. (2018). Single Cell and Open Chromatin Analysis Reveals Molecular Origin of Epidermal Cells of the Skin. Dev. Cell *47*, 133. https://doi.org/10.1016/j.devcel.2018.09.019.

Hnisz, D., Abraham, B.J., Lee, T.I., Lau, A., Saint-André, V., Sigova, A.A., Hoke, H.A., and Young, R.A. (2013). Super-enhancers in the control of cell identity and disease. Cell *155*, 934–947. https://doi.org/10.1016/j.cell.2013.09.053.

Huang, H., Liu, J., An, F., Wu, S., Guo, H., Wang, B., Mo, K., Huang, Y., Tan, J., Zhu, J., et al. (2024). Retinoic acid drives surface epithelium fate determination through the TCF7-MSX2 axis. Cell. Mol. Life Sci. *82*, 16. https://doi.org/10.1007/s00018-024-05525-4.

Huang, H., Liu, J., Li, M., Guo, H., Zhu, J., Zhu, L., Wu, S., Mo, K., Huang, Y., Tan, J., et al. (2022). Cis-regulatory chromatin loops analysis identifies GRHL3 as a master regulator of surface epithelium commitment. Sci. Adv. *8*, eabo5668. https://doi.org/10.1126/sciadv.abo5668.

Itin, P.H. (2014). Etiology and pathogenesis of ectodermal dysplasias. Am. J. Med. Genet. *164a*, 2472–2477. https://doi.org/10.1002/ajmg.a.36550.

Jiang, H., Shukla, A., Wang, X., Chen, W.Y., Bernstein, B.E., and Roeder, R.G. (2011). Role for Dpy-30 in ES cell-fate specification by regulation of H3K4 methylation within bivalent domains. Cell *144*, 513–525. https://doi.org/10.1016/j.cell.2011.01.020.

Jones, K.B., and Klein, O.D. (2013). Oral epithelial stem cells in tissue maintenance and disease: the first steps in a long journey. Int. J. Oral Sci. *5*, 121–129. https://doi.org/10.1038/ijos.2013.46.

Kicheva, A., and Briscoe, J. (2023). Control of Tissue Development by Morphogens. Annu. Rev. Cell Dev. Biol. *39*, 91–121. https://doi.org/10.1146/annurev-cellbio-020823-011522.

Koster, M.I., and Roop, D.R. (2007). Mechanisms regulating epithelial stratification. Annu. Rev. Cell Dev. Biol. *23*, 93–113. https://doi.org/10.1146/annurev.cellbio.23.090506.123357.

Kowalczyk-Quintas, C., and Schneider, P. (2014). Ectodysplasin A (EDA) - EDA receptor signalling and its pharmacological modulation. Cytokine Growth Factor Rev. *25*, 195–203. https://doi.org/10.1016/j.cytogfr.2014.01.004.

LeBlanc, L., Kim, M., Kambhampati, A., Son, A.J., Ramirez, N., and Kim, J. (2022). β-catenin links cell seeding density to global gene expression during mouse embryonic stem cell differentiation. iScience *25*, 103541. https://doi.org/10.1016/j.isci.2021.103541.

Li, H., and Durbin, R. (2010). Fast and accurate long-read alignment with Burrows-Wheeler transform. Bioinformatics *26*, 589–595. https://doi.org/10.1093/bioinformatics/btp698.

Li, L., Wang, Y., Torkelson, J.L., Shankar, G., Pattison, J.M., Zhen, H.H., Fang, F., Duren, Z., Xin, J., Gaddam, S., et al. (2019). TFAP2C- and p63-Dependent Networks Sequentially Rearrange Chromatin Landscapes to Drive Human Epidermal Lineage Commitments. Cell Stem Cell *24*, 271–284.e8. https://doi.org/10.1016/j.stem.2018.12.012.

Link, W. (2019). Introduction to FOXO Biology. Methods Mol. Biol. *1890*, 1–9. https://doi.org/10.1007/978-1-4939-8900-3_1.

Liu, S., Zhang, H., and Duan, E. (2013). Epidermal development in mammals: key regulators, signals from beneath, and stem cells. Int. J. Mol. Sci. *14*, 10869–10895. https://doi.org/10.3390/ijms140610869.

Love, M.I., Huber, W., and Anders, S. (2014). Moderated estimation of fold change and dispersion for RNA-seq data with DESeq2. Genome Biol. *15*, 550. https://doi.org/10.1186/s13059-014-0550-8.

Lwigale, P.Y. (2015). Corneal Development: Different Cells from a Common Progenitor. Prog. Mol. Biol. Transl. Sci. *134*, 43–59. https://doi.org/10.1016/bs.pmbts.2015.04.003.

Nakanoh, S., Sham, K., Ghimire, S., Mohorianu, I., Rayon, T., and Vallier, L. (2024). Human surface ectoderm and amniotic ectoderm are sequentially specified according to cellular density. Sci. Adv. *10*, eadh7748. https://doi.org/10.1126/sciadv.adh7748.

Petrof, G., Nanda, A., Howden, J., Takeichi, T., McMillan, J.R., Aristodemou, S., Ozoemena, L., Liu, L., South, A.P., Pourreyron, C., et al. (2014). Mutations in GRHL2 result in an autosomal-recessive ectodermal Dysplasia syndrome. Am. J. Hum. Genet. *95*, 308–314. https://doi.org/10.1016/j.ajhg.2014.08.001.

Ramírez, F., Ryan, D.P., Grüning, B., Bhardwaj, V., Kilpert, F., Richter, A.S., Heyne, S., Dündar, F., and Manke, T. (2016). deepTools2: a next generation web server for deep-sequencing data analysis. Nucleic Acids Res. *44*, W160–W165. https://doi.org/10.1093/nar/gkw257.

Rauner, G., and Kuperwasser, C. (2021). Microenvironmental control of cell fate decisions in mammary gland development and cancer. Dev. Cell *56*, 1875–1883. https://doi.org/10.1016/j.devcel.2021.06.016.

Rhodes, C.S., Yoshitomi, Y., Burbelo, P.D., Freese, N.H., Nakamura, T., NIDCD/NIDCR Genomics and Computational Biology Core, Chiba, Y., and Yamada, Y. (2021). Sp6/Epiprofin is a master regulator in the developing tooth. Biochem. Biophys. Res. Commun. *581*, 89–95. https://doi.org/10.1016/j.bbrc.2021.10.017.

Ruspita, I., Das, P., Xia, Y., Kelangi, S., Miyoshi, K., Noma, T., Snead, M.L., D'Souza, R.N., and Bei, M. (2020). An Msx2-Sp6-Follistatin Pathway Operates During Late Stages of Tooth Development to Control Amelogenesis. Front. Physiol. *11*, 582610. https://doi.org/10.3389/fphys.2020.582610.

Shukla, V., Cetnarowska, A., Hyldahl, M., and Mandrup, S. (2022). Interplay between regulatory elements and chromatin topology in cellular lineage determination. Trends Genet. *38*, 1048–1061. https://doi.org/10.1016/j.tig.2022.05.011.

Spitz, F., and Furlong, E.E.M. (2012). Transcription factors: from enhancer binding to developmental control. Nat. Rev. Genet. *13*, 613–626. https://doi.org/10.1038/nrg3207.

Subramanian, A., Tamayo, P., Mootha, V.K., Mukherjee, S., Ebert, B.L., Gillette, M.A., Paulovich, A., Pomeroy, S.L., Golub, T.R., Lander, E.S., and Mesirov, J.P. (2005). Gene set enrichment analysis: a knowledge-based approach for interpreting genome-wide

expression profiles. Proc. Natl. Acad. Sci. USA *102*, 15545–15550. https://doi.org/10.1073/pnas.0506580102.

Van Otterloo, E., Milanda, I., Pike, H., Thompson, J.A., Li, H., Jones, K.L., and Williams, T. (2022). AP-2α and AP-2β cooperatively function in the craniofacial surface ectoderm to regulate chromatin and gene expression dynamics during facial development. Elife *11*, e70511. https://doi.org/10.7554/eLife.70511.

Vilchez, D., Boyer, L., Lutz, M., Merkwirth, C., Morantte, I., Tse, C., Spencer, B., Page, L., Masliah, E., Berggren, W.T., et al. (2013). FOXO4 is necessary for neural differentiation of human embryonic stem cells. Aging Cell *12*, 518–522. https://doi.org/10.1111/acel.12067.

Vilchez, D., Boyer, L., Morantte, I., Lutz, M., Merkwirth, C., Joyce, D., Spencer, B., Page, L., Masliah, E., Berggren, W.T., et al. (2012). Increased proteasome activity in human embryonic stem cells is regulated by PSMD11. Nature *489*, 304–308. https://doi.org/10.1038/nature11468.

Whyte, W.A., Orlando, D.A., Hnisz, D., Abraham, B.J., Lin, C.Y., Kagey, M.H., Rahl, P.B., Lee, T.I., and Young, R.A. (2013). Master transcription factors and mediator establish super-enhancers at key cell identity genes. Cell *153*, 307–319. https://doi.org/10.1016/j.cell.2013.03.035.

Wingett, S.W., and Andrews, S. (2018). FastQ Screen: A tool for multi-genome mapping and quality control. F1000Res. *7*, 1338. https://doi.org/10.12688/f1000research.15931.2.

Wu, D.Y., Bittencourt, D., Stallcup, M.R., and Siegmund, K.D. (2015). Identifying differential transcription factor binding in ChIP-seq. Front. Genet. *6*, 169. https://doi.org/10.3389/fgene.2015.00169.

Yu, G., Wang, L.G., Han, Y., and He, Q.Y. (2012). clusterProfiler: an R package for comparing biological themes among gene clusters. OMICS A J. Integr. Biol. *16*, 284–287. https://doi.org/10.1089/omi.2011.0118.

Yu, K., Huang, C., Wan, F., Jiang, C., Chen, J., Li, X., Wang, F., Wu, J., Lei, M., and Wu, Y. (2023). Structural insights into pathogenic mechanism of hypohidrotic ectodermal dysplasia caused by ectodysplasin A variants. Nat. Commun. *14*, 767. https://doi.org/10.1038/s41467-023-36367-6.

Zaret, K.S. (2020). Pioneer Transcription Factors Initiating Gene Network Changes. Annu. Rev. Genet. *54*, 367–385. https://doi.org/10.1146/annurev-genet-030220-015007.

Zhang, J., Sun, Q., Liu, L., Yang, S., Zhang, X., Miao, Y.L., and Liu, X. (2025). Histone methyltransferases MLL2 and SETD1A/B play distinct roles in H3K4me3 deposition during the transition from totipotency to pluripotency. EMBO J. *44*, 437–456. https://doi.org/10.1038/s44318-024-00329-5.

Zhang, Y., Liu, T., Meyer, C.A., Eeckhoute, J., Johnson, D.S., Bernstein, B.E., Nusbaum, C., Myers, R.M., Brown, M., Li, W., and Liu, X.S. (2008). Model-based analysis of ChIP-Seq (MACS). Genome Biol. *9*, R137. https://doi.org/10.1186/gb-2008-9-9-r137.